Utilizing dynamic tensiometry to quantify contact angle hysteresis and wetting state transitions on nonwetting surfaces

Justin A. Kleingartner,[†] Siddarth Srinivasan,[†] Joseph M. Mabry,[‡] Robert E. Cohen,[†] and Gareth H. McKinley*[§]*

[†]Department of Chemical Engineering and [§]Department of Mechanical Engineering, Massachusetts Institute of Technology, Cambridge, Massachusetts 02139, United States of America, and [‡]Air Force Research Laboratory, Edwards Air Force Base, California, United States of America

KEYWORDS Wilhelmy balance, Contact angle hysteresis, Hierarchical structures, Superhydrophobic surfaces, Superoleophobic surfaces, Cassie-Baxter/Wenzel wetting transition.

ABSTRACT

Goniometric techniques traditionally quantify two parameters, the advancing and receding contact angles, that are useful for characterizing the wetting properties of a solid surface; however, dynamic tensiometry, which measures changes in the net force on a surface during the repeated immersion and emersion of a solid into a probe liquid, can provide further insight into the wetting properties of a surface. We detail a framework for analyzing tensiometric results that

allows for the determination of wetting hysteresis, wetting state transitions and characteristic topographical length scales on textured, nonwetting surfaces, in addition to the more traditional measurement of apparent advancing and receding contact angles. Fluorodecyl POSS, a low-surface-energy material, was blended with commercially available poly(methyl methacrylate) (PMMA) and then dip- or spray-coated onto glass substrates. These surfaces were probed with a variety of liquids to illustrate the effects of probe liquid surface tension, solid surface chemistry, and surface texture on the apparent contact angles and wetting hysteresis of nonwetting surfaces. Woven meshes were then used as model structured substrates to add a second, larger length scale for the surface texture. When immersed into a probe liquid, these spray-coated mesh surfaces can form a metastable, solid-liquid-air interface on the largest length scale of surface texture. The increasing hydrostatic pressure associated with progressively greater immersion depths disrupts this metastable, composite interface and forces penetration of the probe liquid into the mesh structure. This transition is marked by a sudden change in the wetting hysteresis, which can be systematically probed using spray-coated, woven meshes of varying wire radius and spacing. We also show that dynamic tensiometry can accurately and quantitatively characterize topographical length scales that are present on micro-textured surfaces.

Introduction

Extremely nonwetting surfaces have attracted great interest for their potential in many commercial and industrial applications, such as self-cleaning,[1-4] drag reduction,[5, 6] and oil-water separation.[7-9] To facilitate the design of nonwetting surfaces, which have apparent advancing contact angles $\theta^* > 90°$, accurate and reliable methods for the characterization of both static and dynamic surface wetting properties are necessary. Goniometric techniques are most frequently used to characterize surface wetting properties, but they suffer from significant measurement

variability when quantifying high apparent contact angles ($\theta^* > 160°$) as a result of gravity-induced sagging that leads to challenges in imaging the meniscus as $\theta^* \to 180°$.[10-12] Several studies have been carried out to compare the accuracy and precision of various tensiometric and goniometric methods,[13, 14] but no universally accepted best method has emerged for measuring liquid contact angles.[15-20] In this work, we explore a framework for analyzing tensiometric results and investigate the utility of dynamic tensiometry as a means to probe wetting state transitions, wetting hysteresis and the role of different topographical length scales on nonwetting surfaces.

Typically a range of contact angle values is observed for a given probe liquid on a smooth solid surface, bounded by the advancing (θ_{adv}) and receding (θ_{rec}) contact angles.[14, 21, 22] The difference between these bounds is the contact angle hysteresis ($CAH = \cos\theta_{rec} - \cos\theta_{adv}$). For the case of a textured solid surface, the wetting behavior of a selected probe liquid depends on both the solid surface energy and the surface roughness.[1, 2, 23-30] When the solid surface energy is low and the surface exhibits re-entrant topography, extremely nonwetting surfaces with very high apparent contact angles ($\theta^*_{adv} > 150°$) and low contact angle hysteresis ($\theta^*_{adv} - \theta^*_{rec} < 10°$) can be obtained for a wide range of liquid surface tensions.[8, 31, 32] In general, a probe liquid can interact with surface texture (altering the apparent contact angle from the flat surface equilibrium value, θ_{eq}, predicted by Young[33]) in one of two ways:[2] imbibition of the probe liquid into the texture (the Wenzel[25] state) or formation of a composite, solid-liquid-air interface on the texture (the Cassie-Baxter[26] state). The Cassie-Baxter state can often be visually observed through the reflective nature of the trapped air layer or 'plastron' on a textured surface.[34] Droplets of probe liquid that sit on the surface in the Wenzel state pin more readily than those in the Cassie-Baxter

state, resulting in increased surface adhesion and consequently increased contact angle hysteresis.[1]

The conditions controlling the transition between the Cassie-Baxter and Wenzel states depend on both the surface chemistry and the length scale of the surface texture.[2, 3] It is now widely recognized[35, 36] that properly applying a smaller length scale of texture on top of a larger textural structure (creating hierarchical textural elements) [37] leads to the formation of more robust nonwetting states. This is illustrated in Figure 1 with a steel mesh that has been spray-coated with a low surface energy coating[38] to create a two-length scale structure, which has then been immersed in water. The plastron is clearly visible as a silvery film. The increase in hydrostatic pressure with immersion depth causes a wetting transition on the larger length scale of the mesh, while a finer scale 'micro-plastron' remains on the individual wires of the mesh and is stabilized by contact line pinning on the finer-scale sprayed structure. Similar transitions between micro- and nano-Cassie-Baxter states have been documented on other hierarchically-textured surfaces.[39] Probing and quantifying such transitions through a single measurement of an integrated quantity, such as an apparent contact angle (θ^*), is clearly insufficient. In the present work we develop a quantitative analysis of the net tensile force exerted by a liquid on a plate, mesh, or other object during an immersion and emersion cycle, and we explain the sequence of observed force transitions expected as the plastron (characterizing the Cassie-Baxter state) is progressively displaced with increasing immersion depth.

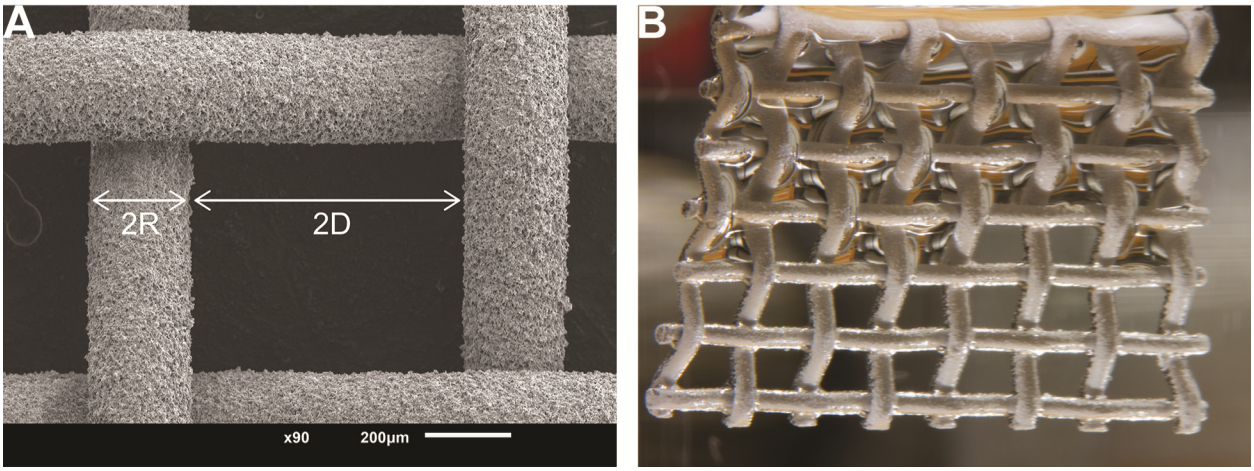

Figure 1. (A) SEM image of a spray-coated stainless steel mesh ($R = 127$ µm and $D = 330$ µm) which forms a surface with hierarchical texture (scale bar $= 200$ µm). The sprayed corpuscles have a droplet diameter $d \approx 20$ µm .[38] (B) Spray-coated mesh undergoing a transition from the Cassie-Baxter to the Wenzel regime on the largest textural length scale. A 'macro-plastron' is observable until the hydrostatic pressure forces a wetting state transition on the largest (mesh) scale. A 'micro-plastron' (indicating a Cassie-Baxter state on the smaller textural length scale) is still observable on the individual, spray-coated wires of the mesh.

Stability of wetting states

A free energy analysis of a liquid drop on a solid surface shows that there is a critical equilibrium contact angle for a given solid-liquid system below (above) which liquid drops are in a thermodynamically stable Wenzel (Cassie-Baxter) state.[1, 8, 40-42] However, metastable Cassie-Baxter drops can also be observed for contact angles less than the critical value.[1, 28, 29] Perturbations to metastable Cassie-Baxter interfaces, such as externally imposed vibrations or pressure perturbations, can force an irreversible transition to the Wenzel regime.[1, 43] A dimensionless parameter A^* has been developed to quantify the resistance of a textured surface to this transition.[31, 42, 44] The magnitude of A^* is a direct measure of the robustness of the metastable Cassie-Baxter interface to a Wenzel transition. This dimensionless robustness parameter is the ratio of the 'breakthrough pressure' Δp_b (*i.e.*, the external pressure difference required to disrupt the Cassie-Baxter interface and cause imbibition of the probe liquid into the

surface texture) and a characteristic reference pressure $p_{ref} = 2\gamma_{lv}/\ell_{cap}$, where $\ell_{cap} = \sqrt{\gamma_{lv}/\rho_l g}$ is the capillary length of the liquid, γ_{lv} is the liquid-vapor surface tension, ρ_l is the probe liquid density, and g is the gravitational acceleration. For the simplest case of a periodic, cylindrical surface texture with a single characteristic length scale ($2R$ in Figure 1a) the robustness parameter is given by the following expression:[42]

$$A^* = \frac{\Delta p_b}{p_{ref}} = \frac{\ell_{cap}}{R(D^* - 1)}\left[\frac{1-\cos\theta}{D^* - 1 + 2\sin\theta}\right] \quad (1)$$

where R is the radius of the cylindrical features, D is half the intercylinder spacing, θ is the three-phase contact angle and $D^* = (R + D)/R$ is the dimensionless spacing ratio of the texture.

Large values of A^* correlate to highly robust Cassie-Baxter interfaces with large breakthrough pressures (or, equivalently, large breakthrough depths $x_b = \Delta p_b/\rho_l g$ when immersed in a vessel of liquid with density ρ_l). As the value of the robustness parameter passes through unity the composite interface is disrupted and spontaneous imbibition of the probe liquid into the texture is expected. The simple 1-D cylindrical model for A^* given above in equation (1) has been shown to be effective in understanding the pressure difference required to disrupt a metastable Cassie-Baxter interface on woven, wire meshes,[44] and these structures are used in the present work as a canonical example of a hierarchical, textured surface being immersed in a liquid.

Solution spraying[38] of woven, wire meshes produces extremely nonwetting surfaces with two well-defined and distinct textural length scales. The hierarchical texture allows structured surfaces to exhibit liquid repellency even when moderately wettable surface chemistries are employed.[32, 37, 45, 46] We use such surfaces to enable systematic investigation of wetting

transitions on multiple length scales. Previously, wetting state transitions have been studied on dip-coated, woven meshes using goniometric techniques by systematically varying the mesh spacing and the probe liquid surface tension;[7, 42, 44, 47] however, dynamic tensiometry permits the controlled imposition of a wetting state transition for a given mesh/liquid combination through an immersion and subsequent emersion cycle.

Dynamic tensiometry of nonwetting surfaces

In a Wilhelmy plate tensiometer, a solid sample is suspended from a sensitive micro-balance and a container of probe liquid is raised and lowered at a constant velocity around the sample while the axial force, $F(t)$, acting on the sample and the sample position, $x(t)$, relative to the free surface datum are measured. A comprehensive analysis for the full immersion and emersion of a nonwetting and wetting plate in a low viscosity fluid is given by Chappuis and Georges.[48] A schematic representing a partially immersed plate with a nonwetting surface is shown in Figure 2.

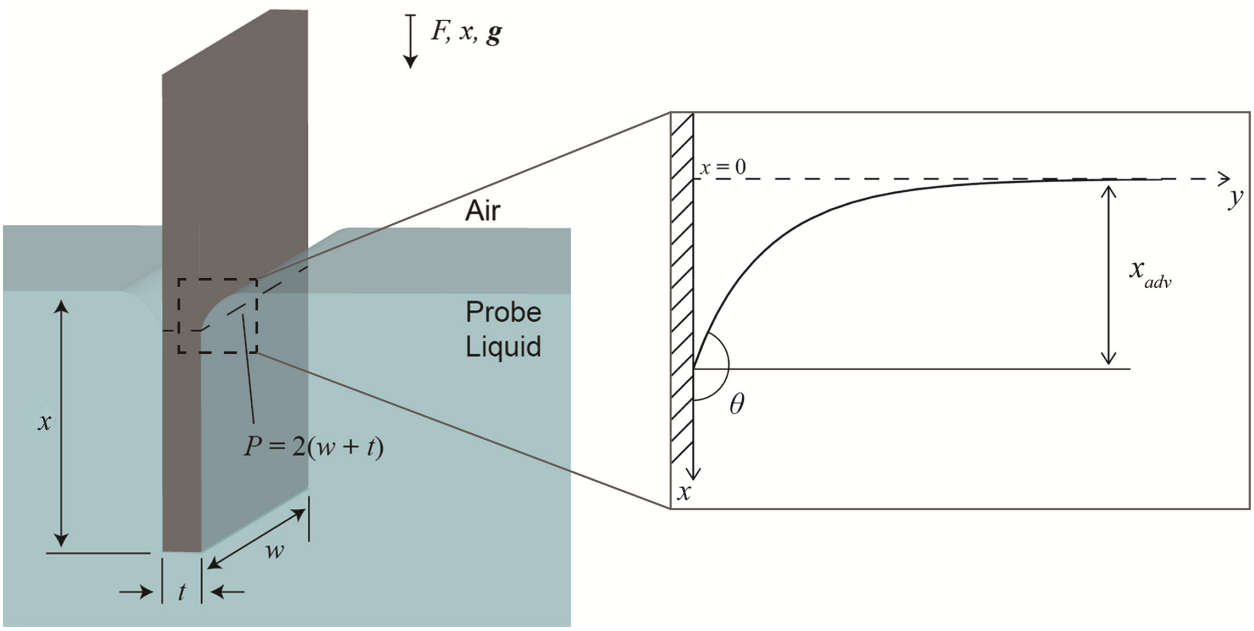

Figure 2. Dynamic tensiometer schematic for a nonwetting surface ($\theta > 90°$). Note that positive force and position are co-aligned with the gravitational acceleration in the downward direction.

In general, three forces are at play in the tensiometer system: interfacial, viscous, and buoyant. For small values of the capillary number ($Ca = \mu U / \gamma_{lv} << 1$, where $U = \dot{x}$ is the immersion velocity and μ is the liquid viscosity) the effect of viscous shear stress exerted by the fluid on the surface of the wetted solid can be neglected.[49] As a result, the net force on a sample in the tensiometer system is $F = P\gamma_{lv}\cos\theta^* - \rho_l g A x$, where $P = 2\left(t + w\right)$ is the length of the solid-liquid-air contact line, $A = tw$ is the cross-sectional area of the solid plate, and x is the immersed depth of the solid. Although interpretation of wetting hysteresis data is clearest when the planar test substrates being immersed are textured or chemically treated on both sides, in principle, the sensitivity of the force transducer makes it possible to probe changes in the contact angle hysteresis for surfaces that are patterned on a single side only.[50] In this case two separate measurements need to be made: one for the untextured test substrate followed by an identical immersion/emersion cycle on the substrate after patterning/surface treatment. The difference

between the two signals is a measure of the changes in the wetting characteristics that are induced by the surface treatment.

To enable comparison of different surfaces and liquids the resultant tensiometric force can be scaled by $P\gamma_{lv}$, which is the magnitude of the maximum interfacial force in the vertical direction (occurring when $\theta^* = 0°$ or $180°$). Likewise, it is appropriate to scale the immersion depth x by $\sqrt{2}\ell_{cap}$, the maximum height of the meniscus, which occurs when $\theta^* = 0°$ or $180°$. This scaling yields the dimensionless force balance

$$\hat{F} = \cos\theta^* - B\hat{x} \tag{2}$$

where $\hat{F} = F/P\gamma_{lv}$ is the nondimensionalized force, $\hat{x} = x/\sqrt{2}\ell_{cap}$ is the nondimensionalized immersion depth, and $B = \sqrt{2}A/P\ell_{cap}$ is a dimensionless group characterizing the magnitude of the buoyant force in the system. For $B << 1$ (e.g., thin fibers or very thin sheets for which $A << P\ell_{cap}$) the buoyant force can be neglected,[51] but this is not the case in the present work.

A force trace, $\hat{F}(\hat{x})$, for an immersion/emersion cycle with a model nonwetting surface is shown in Figure 3.

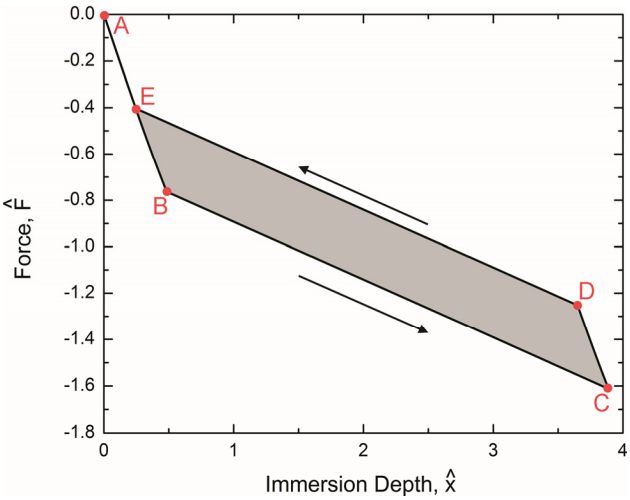

Figure 3. Model of the dimensionless force trace for an ideal solid sample with advancing and receding water contact angles of 130° and 110°, respectively, and $B = 0.25$. Line segment AB corresponds to the formation of the nonwetting meniscus with the contact line pinned at the leading edge of the immersing sample. At B the contact angle reaches the advancing value and the contact line depins. The sample immerses into the probe liquid from B to C with an apparent contact angle θ^*_{adv}. The direction is reversed at C and the contact line pins while the contact angle decreases to the receding value, θ^*_{rec}, which is achieved at point D. Line segment DE represents the equilibrium emersion of the sample from the liquid with $\theta^* = \theta^*_{rec}$. The contact line pins on the leading edge of the solid sample at E and the contact angle decreases below the receding angle until the sample emerges beyond the surface of the probe liquid. The shaded region denotes the wetting hysteresis, $\mathscr{H}$.

We first seek to describe the separate physical processes that govern the shape of this curve and the locus of points $\overrightarrow{ABCDEA}$. When a nonwetting surface first contacts the probe fluid in the tensiometer, the liquid pins on the advancing edge of the solid and the meniscus bends as indicated in Figure 2. Because the surface is nonwetting we expect $\theta^* > 90°$ and the initial tensile force from equation (2) is thus negative, $\hat{F} < 0$. The resultant force during initial development of the meniscus is $\hat{F} = \cos\theta^*(\hat{x}) - B\hat{x}$, which is shown as segment AB in Figure 3. The instantaneous contact angle, $\theta^*(\hat{x})$, can be determined from the shape of the meniscus in contact with the vertically aligned solid and is given by (full derivation provided in the Supporting Information):

$$\theta^*(\hat{x}) = 180° - \arcsin\left[1 - \hat{x}^2\right] \tag{3}$$

The meniscus curvature increases until the instantaneous contact angle, $\theta^*(\hat{x})$, increases to the value of the advancing contact angle, θ^*_{adv}, at which point the interface depins from the advancing edge, and a steady advancing state is subsequently observed with a constant value of meniscus deflection, x_{adv} (Figure 2). The submerged depth at which the contact line depins and begins to advance is given by rearrangement of equation (3):

$$\hat{x}_{adv} = \sqrt{1 - \sin\theta^*_{adv}} \tag{4}$$

The slope of the tensiometric force trace at this point is obtained by evaluating the derivative of the force, given in equation (2) at $x = \hat{x}_{adv}$ (where $\theta^*(\hat{x}) = \theta^*_{adv}$):

$$\left.\frac{d\hat{F}}{d\hat{x}}\right|_{\theta^*=\theta^*_{adv}} = \frac{-2\sin\theta^*_{adv}}{\sqrt{1+\sin\theta^*_{adv}}} - B\,. \tag{5}$$

Therefore, for a surface with $\theta^* > 90°$ the maximum (least negative) slope of the force trace occurs at the moment of depinning and can be no greater than $-B$, which is the value of $\frac{d\hat{F}}{d\hat{x}}$ when $\theta^*_{adv} = 180°$.

Once the contact line depins, a linear relationship for the force $\hat{F}_{adv} = \cos\theta^*_{adv} - B\hat{x}$ (segment BC in Figure 3) is obtained. Upon switching from immersion to emersion (point C in Figure 3), the contact line again becomes pinned resulting in a transient period during which the contact angle decreases from the advancing value to the receding value (segment CD in Figure 3). Once the contact angle reaches the receding angle, $\theta^*(\hat{x}) \to \theta^*_{rec}$, the contact line again depins and the resulting force varies linearly during the emersion phase $\hat{F}_{rec} = \cos\theta^*_{rec} - B\hat{x}$ (segment DE in Figure 3).

The advancing and receding contact angles for a flat, nonwetting substrate can thus be extracted by fitting the steady advancing and receding force balances to the linear portions of the immersion (segment BC) and emersion (segment DE) force traces, respectively. However, for textured surfaces where the wetted perimeter is not known, equation (4) can be used to determine the apparent advancing contact angle and concomitantly provide an estimate of the wetted perimeter (*i.e.*, the length of the three-phase contact line) upon rescaling of the linear advancing force data. Dynamic tensiometry also allows for the clear visualization of wetting hysteresis (shaded region in Figure 3). This quantity can be defined as the area enclosed by the tensiometry curves and evaluated as follows:

$$\begin{aligned} \mathscr{H} &\equiv \frac{\sqrt{2}\ell_{cap}}{L}\oint \hat{F}d\hat{x} \\ &= \frac{1}{\left(\hat{x}_2-\hat{x}_1\right)}\left[\int_{\hat{x}_1}^{\hat{x}_2} F_{em}(\hat{x})d\hat{x} - \int_{\hat{x}_1}^{\hat{x}_2} F_{im}(\hat{x})d\hat{x}\right] \end{aligned} \tag{6}$$

where $\hat{F}_{em}(\hat{x})$ and $\hat{F}_{im}(\hat{x})$ are the experimental force traces measured during emersion and immersion, respectively, and $L = x_2 - x_1$ is the distance over which the hysteresis is computed (typically, but not always, corresponding to the maximum immersion depth). For an ideal tensiometric system, such as that shown in Figure 3 with linear segments BC and DE, equation (6) can be reduced to the familiar definition[52] of contact angle hysteresis $\mathscr{H} = \cos\theta_{rec} - \cos\theta_{adv}$. However, equation (6) can be applied much more generally; specifically, if wetting/dewetting transitions take place at different immersion depths, this will result in measurable changes to the slope of the force-displacement curves as well as changes in the hysteresis of the dynamic wetting process. Tensiometry thus provides a powerful way of probing Cassie-Baxter to Wenzel transitions on textured and patterned surfaces.

Materials and Methods

Materials

The probe liquids used for the wetting/dewetting studies were glycerol (≥99%, Sigma-Aldrich), hexadecane (99%, Sigma-Aldrich) and heptane (99%, Sigma-Aldrich), which were used as received. Deionized water (18.2 MΩ·cm) was purified using a Millipore Milli-Q Academic A10 purification system. Poly(methyl) methacrylate (PMMA, Scientific Polymer Products, M_w = 102 kg mol^{-1} and M_w = 540 kg mol^{-1}) was used as received and 1H,1H,2H,2H-heptadecafluorodecyl polyhedral oligomeric silsesquioxane (fluorodecyl POSS, $\gamma_{sv} \approx 10$ mJ m^{-2}) was synthesized using previously reported protocols.[53] The hydrochlorofluorocarbon solvent Asahiklin AK-225 (Asahi Glass Company) was used to prepare solutions of PMMA and fluorodecyl POSS for dip- and spray-coating applications. Standard (soda lime) glass microscope slides (VWR, 75 mm x 25 mm x 1 mm) and commercially available stainless steel woven meshes (McMaster-Carr) were used as substrates for the dip- and spray-coating processes. The glass microscope slides were cleaned by successive sonication in a 4% (v/v) solution of Micro-90 (International Products Co.), 1 N sodium hydroxide (BDH), and deionized water for 15 minutes prior to coating. The stainless steel woven meshes were coated as received.

Sample Preparation

Cleaned glass microscope slides and stainless steel woven meshes were used as substrates for the spray- and dip-coating processes. To produce the dip-coated samples, the substrates were immersed for 60 minutes in an Asahiklin AK-225 solution of POSS/PMMA followed by 30 minutes of air drying, a second 60 minute immersion, and a final 30 minute drying. The solution contained 20 mg/mL of dissolved solids at a 50/50 POSS/PMMA (M_w = 540 kg mol^{-1}) weight

ratio. The spray coated samples were prepared using a previously reported solution-spraying technique.[38] The spraying solution contained 50/50 (by weight) POSS/PMMA (M_w = 102 kg mol^{-1}) dissolved in Asahiklin AK-225 with 50 mg/ml total dissolved solids.

Surface Characterization

Static contact angle measurements were performed using a ramé-hart Model 590 goniometer. Advancing and receding contact angles were measured optically using the circular-segment-fitting technique with drop volumes of $V \approx 10$ μL . The reported contact angle values represent averages over four or more measurements taken at different locations on the sample with the reported uncertainties representing standard deviations of the measurements. Tensiometric force measurements were made using a DCAT 11 (DataPhysics Instruments) dynamic tensiometer. The glass slide and woven mesh samples were probed at a velocity of U = 0.1 mm/s and U = 0.2 mm/s, and a sampling frequency of 50 Hz and 5 Hz, respectively. All probe liquids were held at 20.0 ± 0.2°C, except for heptane which was held at 2.0 ± 0.2°C to prevent significant evaporation during the time scale of the experiment. The hysteresis $\mathscr{H}$, defined in equation (6), was computed by trapezoidal numerical integration of the experimental tensiometric data. The surface topography of the spray-coated samples was investigated using a JSM-6060 Scanning Electron Microscope (JEOL) operated at an accelerating voltage of 5 kV. The specimens were sputter coated with ~10 nm of gold before imaging. Atomic force microscopy measurements were made in tapping mode with a Dimension 3100 instrument (Veeco Metrology Group).

Results and Discussion

Effects of chemistry and roughness on hysteresis

Surface chemistry and texture play critical and complementary roles in designing robustly nonwetting surfaces. To demonstrate this, we use dip- and spray-coating techniques to systematically control how we impart a low solid-phase surface energy and surface texture to standard glass microscope slides. Two flat surfaces with differing surface chemistries and two chemically-equivalent surfaces (one with a controlled surface texture and one nominally flat surface) were fabricated.

To examine the effects of texture, solutions of 50/50 (by weight) PMMA/POSS solution were either dip- or spray-coated onto glass slide substrates to produce flat and textured surfaces, respectively, with the same low-energy surface chemistry. The tensiometric force traces are compared in Figure 4A and B. The differing slopes of the immersion and emersion lines in Figure 4A and the area enclosed by the curves (shaded region) shows that this flat nonwetting surface exhibits noticeable hysteresis ($\theta_{adv} = 129°$ and $\theta_{rec} = 110°$) even with the extremely low surface energy molecule fluorodecyl POSS coating. However, the addition of micro-texture by applying the PMMA/POSS solution as a spray-on coating promotes the establishment of a stable composite Cassie-Baxter interface which increases the observed advancing and receding contact angle significantly (*i.e.,* the value of the measured force $\hat{F}$ becomes increasingly negative). When the force curve is linearly extrapolated back to the ordinate axis ($\hat{x} = 0$), the value of the intercept, denoted $\hat{F}_0$, is directly related to the apparent contact angle. The contact angle hysteresis on this spray-coated surface also becomes immeasurably small resulting in a super nonwetting surface (Figure 4B).

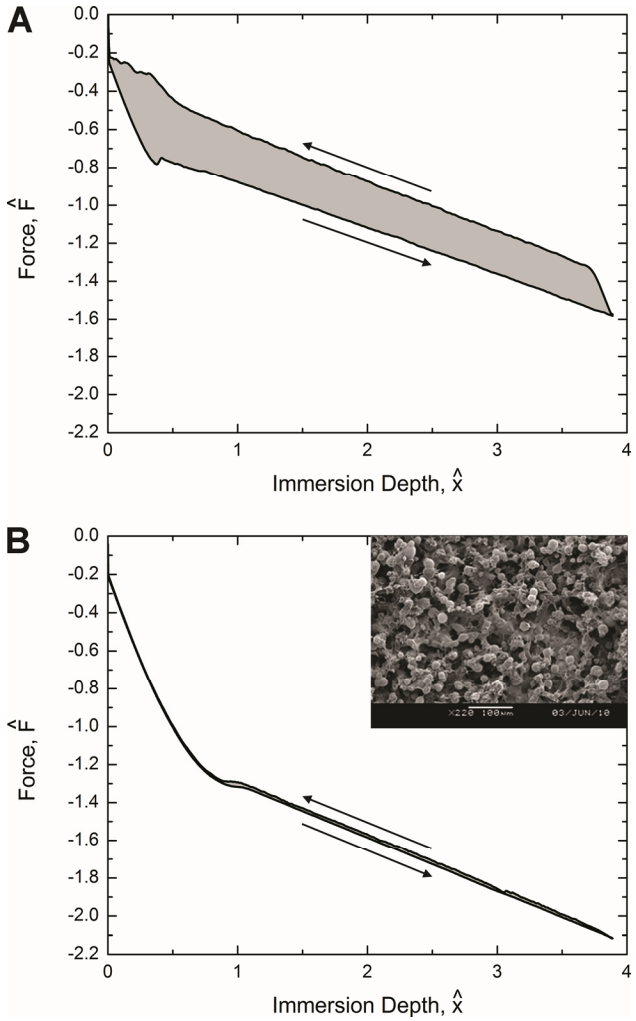

Figure 4. Measured force traces plotted against dimensionless immersion depth for 50/50 (by weight) PMMA/POSS (A) dip-coated and (B) spray-coated glass slides being immersed in water, $\ell_{cap} = 2.73$ mm. The dip-coated surface in (A) was relatively smooth with a root-mean-square roughness of $R_q = 19.5$ nm measured by atomic force microscopy. The inset in (B) is a micrograph of the textured surfaces prepared by spray-coating (scale bar $= 100$ μm).[38]

Using the force balance given in equation (2) and the known surface tension of water $\gamma_{lv} = 72$ mN/m (with the measured macroscopic perimeter of the glass slide $P_{macro} = 52$ mm), both the immersion and emersion data shown in Figure 4B lead to an intercept at $\hat{x} = 0$ of $\hat{F} = -1.02$, which is unphysical because it corresponds to $\cos\theta < -1$. This result suggests that the true value of the wetted perimeter is larger than the nominal macroscopic value; a situation that arises because the three-phase contact line conforms on microscopic length scales to the

tortuous corpuscular texture produced by solution spraying (Inset Figure 4B). To determine the true wetted perimeter, the advancing contact angle can, in principle, be calculated from the position at which the contact line depins (point B in Figure 3). For the experimental force trace shown in Figure 4B identifying a single point at which the contact line depins is unclear, because the depinning is a distributed event in real systems. However, the average position at which the contact line depins can be unambiguously defined as the point of intersection between the force trace during the initial meniscus formation (segment AB in Figure 2) and the straight line that describes the steady advancing portion of the force trace (segment BC). Equation (4) can then be used to determine the apparent advancing contact angle. For the spray-coated slide in Figure 4B this analysis yields an advancing water contact angle of $\theta^*_{adv} = 154°$ (by contrast, $\theta^*_{adv} = 160°$ when determined goniometrically) and thus leads to calculation of the true value of the wetted perimeter, $P_{micro} = 59.3$ mm, which corresponds to a 14% increase over the nominal value obtained from macroscopic measurement of the specimen width and thickness. Dynamic tensiometry can thus be used to measure effective contact angles for extremely nonwetting surfaces where the wetted perimeter is unknown, and this provides insight into the topography traversed by the moving contact line (*i.e.*, the effective tortuosity of the textured coating).

The effects of surface chemistry in the absence of texture were also investigated and are shown in Figure 5 (traces I and II). Two glass slides, one uncoated and the other dip-coated in a 50/50 (by weight) solution of PMMA/POSS present very different surface chemistries. The high surface energy, uncoated glass slide had advancing and receding water contact angles of $\theta_{adv} = \theta_{rec} = 0°$ and the tensile force acting on the slide is thus positive (trace I). The low surface

energy, dip-coated glass slide has large apparent advancing and receding water contact angles of $\theta_{adv} = 129°$ and $\theta_{rec} = 110°$, respectively, and substantial contact angle hysteresis (trace II).

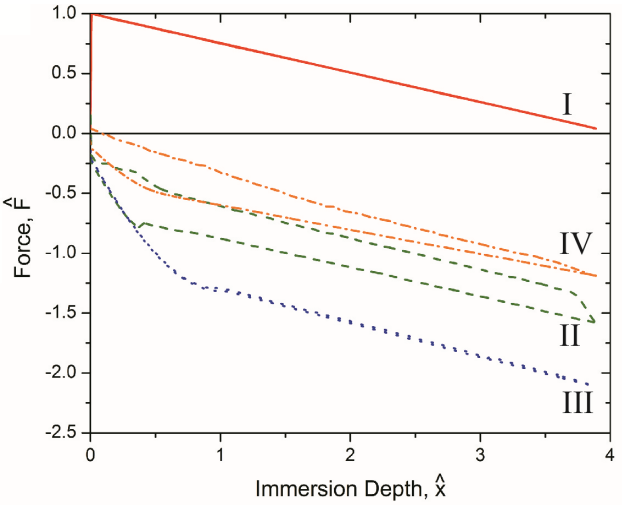

Figure 5. Measured tensile force plotted against immersed depth for a bare glass slide (—, I), a 50/50 (by weight) PMMA/POSS dip-coated glass slide (- - -, II), and a 50/50 (by weight) PMMA/POSS spray-coated glass slide (·····, III) immersed in water and the same spray-coated slide immersed in hexadecane (-·-·-, IV).

Table 1. Goniometric advancing (θ^*_{adv}) and receding (θ^*_{rec}) contact angles, contact angle hysteresis ($CAH = \cos\theta^*_{rec} - \cos\theta^*_{adv}$), and wetting hysteresis ($\mathscr{H}$) for six solid/liquid systems. The tensiometric force traces for systems I - IV are presented in Figure 5.

System	Surface	Liquid	θ^*_{adv} (degrees)	θ^*_{rec} (degrees)	CAH (x 10^{-2})	$\mathscr{H}$ (x 10^{-2})
I	Bare Glass	Water	0	0	0.0	0.3
II	POSS/PMMA Dip-coated	Water	124	118	8.8	24.6
III	POSS/PMMA Spray-coated	Water	159	157	1.3	1.5
IV	POSS/PMMA Spray-coated	Hexadecane	150	125	29.2	16.8
V	POSS/PMMA Dip-coated	Hexadecane	79	73	10.7	27.3
VI	POSS/PMMA Dip-coated	Heptane	63	19	49.2	36.0

The additional force traces III and IV presented in Figure 5 for the low-energy, spray-coated surfaces highlight the effects of liquid surface tension on surface wettability and hysteresis. The increase in contact angle hysteresis (summarized in Table 1) of the textured surface when probed with hexadecane (trace IV) compared to water (trace III) is primarily driven by the lower

robustness (A^*) of the surface to the lower surface tension probe liquid ($\gamma_{hexadecane} = 27.5$ mN/m compared to $\gamma_{water} = 72.8$ mN/m). Less robust Cassie-Baxter interfaces are pushed more deeply into the re-entrant mircro-texture causing them to pin more readily on physical surface heterogeneities and consequently produce greater contact angle hysteresis on emersion. The lower robustness of the Cassie-Baxter state for a hexadecane interface is also most apparent in the nonlinear form of the receding force trace (IV), which results from progressive imbibition of the probe liquid into the surface texture with increasing depth. Near the point of maximum immersion depth ($\hat{x} \approx 3.5$) the instantaneous wetting hysteresis associated with the difference in the dimensionless advancing and receding force is $\left(\hat{F}_{rec} - \hat{F}_{adv}\right)\Big|_{\hat{x}=3.5} = 0.056$. At this instant, the meniscus is located at a surface position (relative to the leading edge) of $x = 13.5$ mm and is receding over textured surface that has not been immersed deeply into the hexadecane. By contrast, at the point $\hat{x} = 1.0$ corresponding to a depth near where the advancing interface first depins, the instantaneous wetting hysteresis is increased fivefold to $\left(\hat{F}_{rec} - \hat{F}_{adv}\right)\Big|_{\hat{x}=1.0} = 0.27$. At this instant, the meniscus is located at a position relative to the leading edge of $x = 3.9$ mm but is now receding over a textured surface that has already been immersed deeply into the fluid.

The integrated effect of these immersion/emersion cycles can be represented by calculating the hysteresis ($\mathscr{H}$) for these surfaces using equation (6). Both the superhydrophilic, bare glass (with extremely low water contact angle) and the extremely nonwetting, highly textured surface exhibit essentially no hysteresis in water (Systems I and III in Table 1 and Figure 5). By contrast, when liquids with intermediate values of surface tension are used to probe the solid surfaces, significant hysteresis is apparent. For textured surfaces, imbibition of the probe liquid (*e.g.*, in system IV) can lead to a dependence of the instantaneous wetting hysteresis on immersion depth.

Effects of multiple textural length scales

To demonstrate the changes in wetting hysteresis that can be induced by adding an additional textural length, we use a commercially available stainless steel mesh (wire radius R = 254 μm, weave half-spacing D = 457 μm) as the substrate for the spray-coating process. We use the resulting two-length scale structure to investigate the stability of the Cassie-Baxter state and the collapse of the macro-plastron film shown in Figure 1. The Cassie-Baxter regime established when the meniscus advances over the surface is often metastable and as a result can be forced to transition irreversibly to the Wenzel regime under an external pressure perturbation.[1] Dynamic tensiometry allows for the systematic investigation of this transition, since the hydrostatic pressure in the system increases with the immersion depth. However, the challenge faced in deconvoluting the information contained in the measured force trace is that it contains two distinct contributions: a buoyancy term that depends on the volume of liquid that is displaced by the immersed sample, and a capillary force associated with the present location of the contact line as it advances over a dry nonwetted surface, or recedes over a surface that has been previously immersed to a user-specified, maximum depth. Prior to reaching the breakthrough depth ($\hat{x}_b$), the observed tensiometric force is described by equation (2): $\hat{F} = \cos\theta^*_{adv} - B_c\hat{x}$, where $B_c = \sqrt{2}A_c \big/ P_c \ell_{cap}$ is a dimensionless measure of the buoyant force, A_c is the effective displaced cross-sectional area in the Cassie-Baxter state, and P_c is the length of the contact line in the Cassie-Baxter state. After breakthrough and collapse of the macro-plastron, the length of the wetted perimeter and the effective cross-sectional area of the immersed sample (that displaces fluid and gives rise to the buoyant force) both change. For the specific case of the periodic mesh, the analysis is somewhat simplified because the mesh interstices are filled with air when it is in the Cassie-Baxter regime (Figure 1) and a fluid volume equivalent to the entire

macroscopic volume of the mesh (consisting of both air and wire) is displaced upon immersion. Therefore, both A_c and P_c can be calculated using the macroscopic dimensions of the rectangular mesh sample. After breakthrough of the composite interface ($\hat{x} > \hat{x}_b$) and collapse of the macroscopic plastron, there is a decrease in the effective displaced volume; the effective cross-sectional area of the sample decreases as a result of the probe liquid penetration into the woven mesh structure. This yields a resultant immersion force after breakthrough given by

$$\hat{F} = \cos\theta - B_c\hat{x}_b - B_w(\hat{x} - \hat{x}_b) \qquad \text{for } \hat{x} > \hat{x}_b \tag{7}$$

where $B_w = \sqrt{2}A_w \big/ P_c \ell_{cap}$ and A_w is the effective cross-sectional area of the sample in the Wenzel regime. We note here that we retain our initial scaling of $\hat{F}$ with the wetted perimeter in the Cassie-Baxter state (P_c) to avoid introducing a discontinuity in the dimensionless force, which would result from the jump in the wetted perimeter at the breakthrough event. The cross-sectional area of the sample in the Wenzel regime, A_w, is computed by averaging the cross-sectional area of the mesh over the immersion depth. Comparing the expected force before and after breakthrough, it is evident that there should be a change in the slope of the immersion force curve at $x = x_b$ of magnitude $\left(B_c - B_w\right)$ due to the change in the effective displaced cross-sectional area ($A_c > A_w$) between the two wetting regimes.

Tensiometry measurements for spray- and dip-coated meshes are shown in Figure 6. The predicted slopes of the force traces (Figure 6A) determined from *a priori* knowledge of the mesh geometry are $B_c = 0.25$ and $B_w = 0.11$ in the Cassie-Baxter and Wenzel regimes, respectively. As a result, the wetting transition is predicted to show only a subtle change in slope for the spray-coated mesh. The values for the experimentally measured buoyancy slopes were $B_c = 0.16$

and $B_w = 0.12$ in the Cassie-Baxter and Wenzel regimes, respectively, which are consistent with the expected trend. The lower than expected value of the dimensionless buoyancy B_c in the Cassie-Baxter state results from the assumption that the effective cross-sectional area (A_c) of the coated mesh can be computed from its macroscopic cross-sectional area. Due to the woven nature of the mesh and sagging of the liquid-air interface into the mesh interstices, the calculated value of A_c actually serves as an upper bound on the value of B_c.

While only a subtle change in the slope of the force trace is expected (and observed) at x_b, there is a very distinct change in the wetting hysteresis at the transition. The part of the mesh that persists in the Cassie-Baxter regime shows noticeably less hysteresis than the portion associated with the Wenzel regime. This is a result of the differences in the wetting dynamics between the composite, solid-liquid-air interface as compared to the solid-liquid Wenzel interface. While receding in the Cassie-Baxter state, the three-phase contact line is only weakly pinned, because the wetted area fraction of the solid is small. Therefore, the meshes initially recede with low hysteresis as the Cassie-Baxter portion emerges from the probe liquid. However, after receding for a distance greater than the breakthrough depth, x_b, the portion of the mesh that is in the Wenzel regime emerges from the liquid reservoir with dramatically increased hysteresis. The experimentally observed breakthrough depths for spray- and dip-coated meshes (with $D = 452$ μm, $R = 254$ μm) were $x_b^{spray} \approx 9.9$ mm and $x_b^{dip} \approx 6.0$ mm, corresponding to breakthrough pressures of $\Delta p_b^{spray} = 97$ Pa and $\Delta p_b^{dip} = 59$ Pa, respectively.

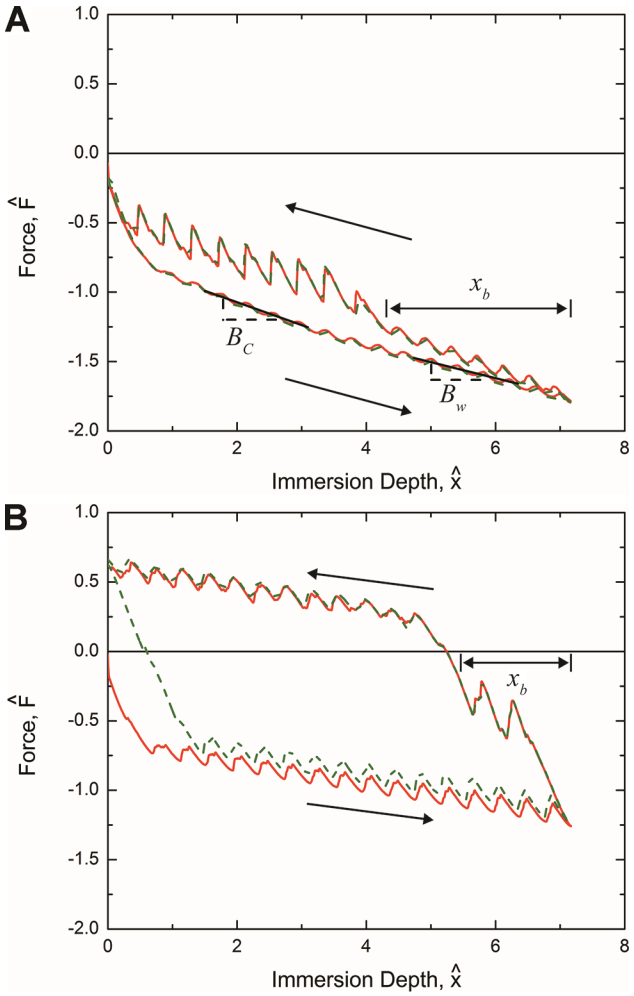

Figure 6. Measured force as a function of immersed depth for (A) a spray-coated and (B) a dip-coated stainless steel mesh ($D = 457$ μm, $R = 254$ μm) immersed in 50/50 (by volume) glycerol/water . Solid red (——) and dashed green (- - -) lines correspond to first and second tensiometric cycles, respectively. The breakthrough depth corresponds to the large jump in the hysteresis of the immersion/emersion force trace. A capillary length of $\ell_{cap} = 2.47$ mm and a maximum interfacial force of $P\gamma_{lv} = 2.12$ mN were used to scale the measured displacement and tensile force, respectively.

The spray- and dip-coated stainless steel woven meshes were used to investigate the wetting transition for two different values of the robustness parameter (defined in equation 1), while maintaining the same overall geometry. The goniometric advancing contact angles for the spray- and dip-coatings on a flat substrate were $\theta^*_{spray} = 160°$ and $\theta^*_{dip} = 124°$, which yield robustness factors for the macroscopic mesh texture of $A^*_{spray} = 4.7$ and $A^*_{dip} = 2.7$, and water breakthrough

depths (of the macro-plastron) of $x_b^{spray} = 25.5$ mm and $x_b^{dip} = 14.5$ mm, respectively. While the absolute values of the breakthrough predictions (corresponding to the condition at which the hydrostatic pressure $\rho_l g x_b$ exceeds the pressure Δp_b from equation 1) deviate slightly from the experimental results, the robustness framework performs well in predicting changes in relative breakthrough depth, which is approximately 1.75 times larger for the spray-coated mesh. This result supports the findings of past work that investigated the qualitative and quantitative predictive power of the robustness parameter A^*.[44]

Hysteresis in the Cassie-Baxter and Wenzel Regimes

Six spray-coated woven meshes (with geometric properties summarized in Table 2) were used to investigate the effect of mesh spacing on the hysteresis and breakthrough depth of a two-length scale textured surface. As the spacing of the mesh increases, the robustness (A^*) of the composite liquid interface on the mesh decreases (equation 1). The consequences of this decrease in robustness have been observed previously using sessile drops of various liquids placed on wire meshes and fabrics.[31, 44] This same trend (Table 2) is observed using a single probe liquid in our dynamic tensiometry experiments presented in Figure 7. The breakthrough event is triggered by steadily increasing the applied pressure difference Δp (or, equivalently, the immersion depth $x = \Delta p / \rho_l g$) acting on the plastron as opposed to progressively reducing the liquid surface tension of different sessile drops that are sequentially placed on the textured surface.

Table 2. The mesh number (number of openings per inch), wire radius (R), weave half-spacing (D), dimensionless spacing ratio (D^*), predicted robustness factor (A^*), experimental breakthrough depth (x_b), and Cassie-Baxter ($\mathscr{H}_c$) and Wenzel ($\mathscr{H}_w$) state hysteresis for spray-coated woven meshes immersed in 50/50 (by volume) glycerol/water. The predicted breakthrough pressure can be determined from the dimensionless robustness A^* as $\Delta p_b = p_{ref} A^*$ (equation 1), where the reference pressure is $p_{ref} = 55$ Pa for this system.

Mesh	R (μm)	D (μm)	D*	A*	x_b (mm)	$\mathscr{H}_c$ (x 10^{-2})	$\mathscr{H}_w$ (x 10^{-2})
40	127	191	2.5	11.5	43.0	4.89	--
28	127	330	3.6	4.4	16.1	7.25	20.5
15	127	724	6.7	1.0	2.5	2.36	42.7
18	254	457	2.8	4.2	9.9	7.59	26.2
12	254	800	4.2	1.6	5.0	5.39	28.4
10	254	1016	5.0	1.0	<2	4.11	39.5

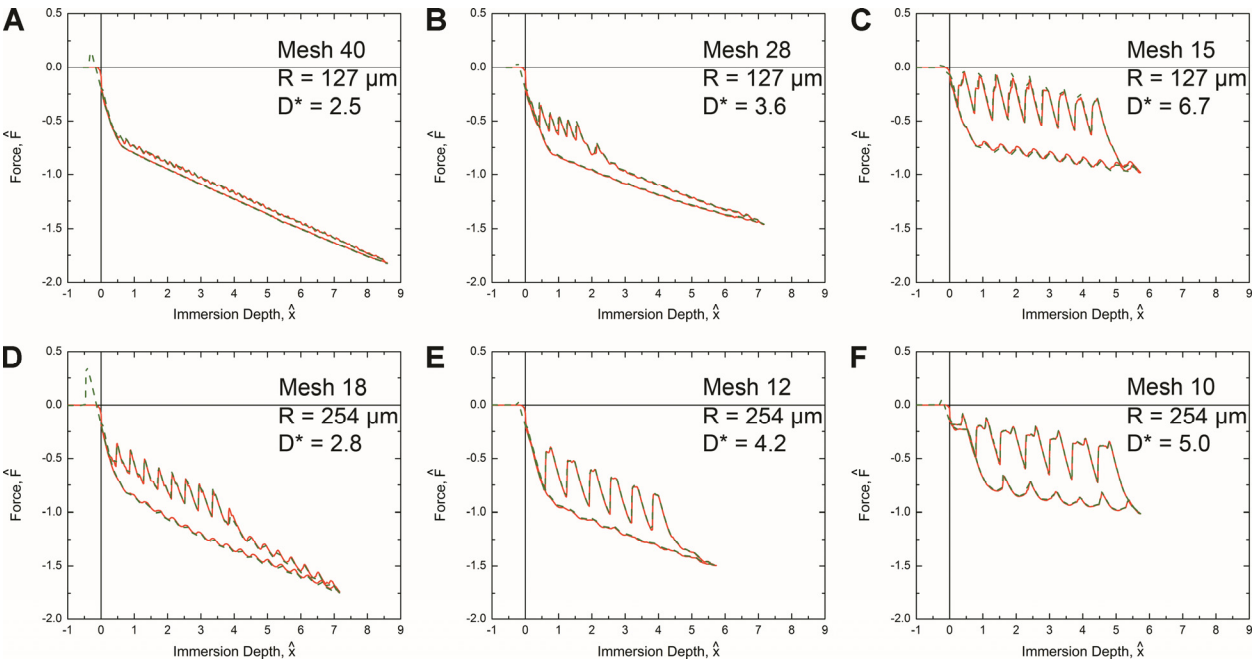

Figure 7. Measured force as a function of immersion depth for six spray-coated meshes (summarized in Table 2) immersed in 50/50 (by volume) glycerol/water. Panels A-C and D-F show the effect of increasing the mesh spacing for fixed wire diameters of R = 127 μm and R = 254 μm, respectively. Solid red (——) and dashed green (- - -) lines correspond to first and second tensiometric cycles, respectively. Through repeated cycling no changes were observed in the measured force traces.

The tensiometric results show that breakthrough occurs at lower pressures as the dimensionless mesh wire spacing D^* increases, or as R increases at constant D^*. For the finest mesh (Mesh 40; $R = 127$ μm) no breakthrough is observed; the plastron remains intact up to the maximum immersion depth and the surface remains in the Cassie-Baxter state throughout the entire immersion/emersion cycle. The pressure-induced transition from the Cassie-Baxter to Wenzel states is most readily observed in tensiometry as a sudden increase in the hysteresis of the tensiometric force trace. The hysteresis in the Cassie-Baxter regime ($\mathscr{H}_c$) and in the Wenzel regime ($\mathscr{H}_w$) can be computed by integration of equation (6) over the portion of the force trace corresponding to each regime of interest. The results are shown graphically in Figure 8 and are tabulated in Table 2.

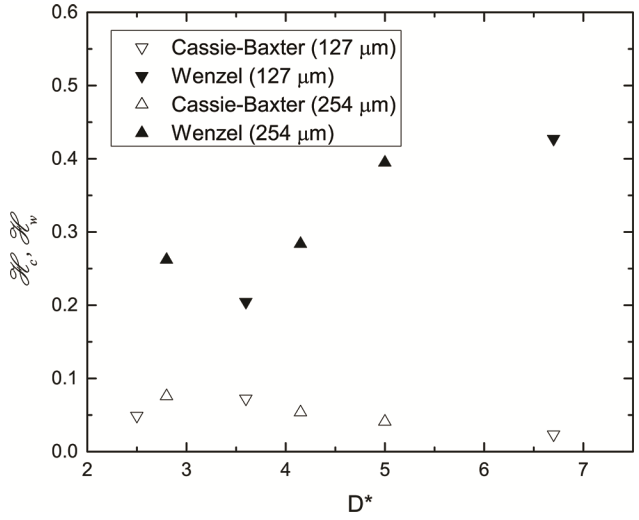

Figure 8. Cassie-Baxter ($\mathscr{H}_c$) and Wenzel ($\mathscr{H}_w$) state hysteresis for spray-coated woven meshes immersed in 50/50 (by volume) glycerol/water. The Wenzel hysteresis for the mesh with $D^* = 2.5$ could not be measured, because the breakthrough depth ($x_b = 43$ mm) was greater than the maximum immersion depth ($x_{\max} \approx 30$ mm) attainable with the tensiometer.

The data clearly reveal the increase in hysteresis that accompanies the transition from the Cassie-Baxter to the Wenzel state ($\mathscr{H}_c < \mathscr{H}_w$). This increase in hysteresis is in good agreement with

previous results reported for metastable Cassie-Baxter interfaces exposed to externally applied pressures.[1, 43] As D^* increases for a given mesh wire radius, the wetted area fraction of solid in the Cassie-Baxter state and the value of $\mathscr{H}_c$ also decreases. By contrast, the value of the hysteresis associated with the Wenzel state increases. For the hierarchically-textured surface (spray-coated mesh), the increase in hysteresis results from an increase in meniscus pinning upon transition from the Cassie-Baxter state to the Wenzel state, and a concomitant increase in the amplitude of the oscillations in the receding force traces after transition.

Quantifying topographical length scales with tensiometry

The stainless steel woven meshes also offer a model periodic texture for investigating characteristic geometric length scales by tensiometry. The force data shown in Figure 7 exhibit regular periodicity in both the immersion and emersion force traces as a result of the liquid meniscus traversing the individual horizontal wires of the spray-coated mesh. To quantify the frequency of these oscillations the measured force data was first detrended (*i.e.*, the effective slope resulting from the buoyancy term in equation (2) was first removed from the data) and a discrete Fourier transform was then used to evaluate the corresponding power spectrum of the fluctuating force signal. The frequency distribution, in conjunction with the experimentally-imposed velocity ($U = 0.2$ mm/s), enables the calculation of the texture periodicity from the primary harmonic of the spectrum. Advancing and receding power spectra gave virtually identical values for the period of the mesh texture (Figure S1 in the Supporting Information) and agreed well with the manufacturer-specified periodicity for the meshes. The high reproducibility of the measurements (shown in Figure 7) across immersion and emersion force traces, and in repeated cycling demonstrates the ability of dynamic wetting measurements to quantify the characteristic geometric length scales of periodic textures without the need for potentially-

destructive microscopic techniques. The resolution of the surface features that can be investigated is limited primarily by the spatial resolution of the displacement stage of the tensiometer, which is less than 1 μm for modern systems.

Conclusions

In this work we have demonstrated the utility of dynamic tensiometry for determining wetting state transitions and topographical length scales on textured nonwetting surfaces, as well as for the more traditional measurement of apparent advancing and receding contact angles. We have shown how dynamic tensiometry can be used to analyze surface topography and obtain an effective wetted perimeter on textured substrates that properly reflects the tortuosity of the advancing or receding three-phase contact line. The wetting hysteresis ($\mathscr{H}$) of a textured surface was defined in terms of the enclosed area between the advancing and receding force traces, which provides additional insight for chemically or physically heterogeneous surfaces beyond the traditional single-point definition of contact angle hysteresis, $CAH = \cos\theta_{rec} - \cos\theta_{adv}$. With respect to the determination of the transition from the metastable Cassie-Baxter regime to the Wenzel regime, only small changes in the overall slope of the advancing force trace are observed, whereas the transition between the wetting states can be detected very clearly in an immersion/emersion cycle by a sudden and pronounced change in the hysteresis. This allows for the ready determination of the breakthrough depth (x_b) from a single tensiometric experiment. The wetting hysteresis, defined by equation (6), is always smaller in the Cassie-Baxter regime than in the Wenzel regime ($\mathscr{H}_c < \mathscr{H}_w$) for hierarchically-textured systems that show a pressure-induced transition between the two regimes. It was also demonstrated that dynamic tensiometric characterization of surface wettability can accurately and reliably probe

the characteristic length scales that are present on micro-textured surfaces, and which control the macroscopically observed hysteresis. Dynamic tensiometry thus provides a rapid and reliable test protocol for more completely characterizing the wetting properties of textured and patterned surfaces.

ASSOCIATED CONTENT

Supporting Information. Derivation of the instantaneous contact angle during the formation of a nonwetting meniscus and the Fourier transform power spectra of the linearly detrended force traces for one of the meshes investigated in this work. This material is available free of charge via the Internet at http://pubs.acs.org.

AUTHOR INFORMATION

Corresponding Author

*E-mail: Robert E. Cohen (recohen@mit.edu) and Gareth H. McKinley (gareth@mit.edu).

Author Contributions

The manuscript was written through contributions of all authors. All authors have given approval to the final version of the manuscript.

ACKNOWLEDGMENT

We gratefully acknowledge financial support from the Air Force Research Laboratory, Propulsion Directorate, the Air Force Office of Scientific Research, and the Army Research Office through contract W911NF-07-D-0004. We thank the Institute for Soldier Nanotechnologies (ISN) at MIT for the use of their SEM, and Mr. Hyomin Lee and Mr. Shreerang Chhatre for helpful discussions during the preparation of this article.

REFERENCES

1. Lafuma, A.; Quéré, D. Superhydrophobic states. *Nat. Mater.* **2003**, 2, 457-460.
2. Quéré, D. Wetting and Roughness. *Ann. Rev. Mater. Res.* **2008**, 38, 71-99.
3. Bhushan, B.; Jung, Y. C. Natural and biomimetic artificial surfaces for superhydrophobicity, self-cleaning, low adhesion, and drag reduction. *Prog. Mater. Sci.* **2011**, 56, 1-108.
4. Park, K.-C.; Choi, H. J.; Chang, C.-H.; Cohen, R. E.; McKinley, G. H.; Barbastathis, G. Nanotextured Silica Surfaces with Robust Superhydrophobicity and Omnidirectional Broadband Supertransmissivity. *ACS Nano* **2012**, 6, 3789-3799.
5. Lee, C.; Kim, C.-J. Underwater Restoration and Retention of Gases on Superhydrophobic Surfaces for Drag Reduction. *Physical Review Letters* **2011**, 106, 014502.
6. Jung, Y. C.; Bhushan, B. Biomimetic structures for fluid drag reduction in laminar and turbulent flows. *J. Phys.: Condens. Matter* **2010**, 22, 035104.
7. Feng, L.; Zhang, Z.; Mai, Z.; Ma, Y.; Liu, B.; Jiang, L.; Zhu, D. A Super-Hydrophobic and Super-Oleophilic Coating Mesh Film for the Separation of Oil and Water. *Angew. Chem. Int. Ed.* **2004**, 43, 2012-2014.
8. Tuteja, A.; Choi, W.; Ma, M. L.; Mabry, J. M.; Mazzella, S. A.; Rutledge, G. C.; McKinley, G. H.; Cohen, R. E. Designing superoleophobic surfaces. *Science* **2007**, 318, 1618-1622.
9. Kota, A. K.; Kwon, G.; Choi, W.; Mabry, J. M.; Tuteja, A. Hygro-responsive membranes for effective oil–water separation. *Nat. Commun.* **2012**, 3, 1025.
10. Dorrer, C.; Ruhe, J. Some thoughts on superhydrophobic wetting. *Soft Matter* **2009**, 5, 51-61.
11. Extrand, C. W.; Moon, S. I. Contact Angles of Liquid Drops on Super Hydrophobic Surfaces: Understanding the Role of Flattening of Drops by Gravity. *Langmuir* **2010**, 26, 17090-17099.
12. Srinivasan, S.; McKinley, G. H.; Cohen, R. E. Assessing the Accuracy of Contact Angle Measurements for Sessile Drops on Liquid-Repellent Surfaces. *Langmuir* **2011**, 27, 13582-13589.
13. Krishnan, A.; Liu, Y. H.; Cha, P.; Woodward, R.; Allara, D.; Vogler, E. A. An evaluation of methods for contact angle measurement. *Colloids Surf., B* **2005**, 43, 95-98.
14. Lander, L. M.; Siewierski, L. M.; Brittain, W. J.; Vogler, E. A. A Systematic Comparison of Contact Angle Methods. *Langmuir* **1993**, 9, 2237-2239.
15. Strobel, M.; Lyons, C. S. An Essay on Contact Angle Measurements. *Plasma Process. Polym.* **2011**, 8, 8-13.
16. Di Mundo, R.; Palumbo, F. Comments Regarding 'An Essay on Contact Angle Measurements'. *Plasma Process. Polym.* **2011**, 8, 14-18.
17. Müller, M.; Oehr, C. Comments on "An Essay on Contact Angle Measurements" by Strobel and Lyons. *Plasma Process. Polym.* **2011**, 8, 19-24.
18. Ruiz-Cabello, F. J. M.; Rodríguez-Valverde, M. A.; Cabrerizo-Vílchez, M. A. Additional Comments on "An Essay on Contact Angle Measurements" by M. Strobel and C. S. Lyons. *Plasma Process. Polym.* **2011**, 8, 363-366.
19. Terriza, A.; Alvarez, R.; Yubero, F.; Borras, A.; González-Elipe, A. R. Comments on "An Essay on Contact Angle Measurements": Determination of Surface Roughness and Modeling of the Wetting Behavior. *Plasma Process. Polym.* **2011**, 8, 998-1002.

20. Kietzig, A.-M. Comments on "An Essay on Contact Angle Measurements" - An Illustration of the Respective Influence of Droplet Deposition and Measurement Parameters. *Plasma Process. Polym.* **2011**, 8, 1003-1009.
21. Gao, L.; McCarthy, T. J. Wetting 101°. *Langmuir* **2009**, 25, 14105-14115.
22. Marmur, A. Contact Angle Hysteresis on Heterogeneous Smooth Surfaces. *J. Colloid Interface Sci.* **1994**, 168, 40-46.
23. Callies, M.; Quéré, D. On water repellency. *Soft Matter* **2005**, 1, 55-61.
24. Marmur, A. The Lotus Effect: Superhydrophobicity and Metastability. *Langmuir* **2004**, 20, 3517-3519.
25. Wenzel, R. N. Resistance of solid surfaces to wetting by water. *Ind. Eng. Chem.* **1936**, 28, 988-994.
26. Cassie, A. B. D.; Baxter, S. Wettability of porous surfaces. *Trans. Faraday Soc.* **1944**, 40, 546-551.
27. Johnson Jr, R. E.; Dettre, R. H. Contact Angle, Wettability and Adhesion. In *Advances in Chemistry Series*, Fowkes, F. M., Ed. American Chemical Society: Washington, 1964; Vol. 43, pp 112-135.
28. Öner, D.; McCarthy, T. J. Ultrahydrophobic Surfaces. Effects of Topography Length Scales on Wettability. *Langmuir* **2000**, 16, 7777-7782.
29. Yoshimitsu, Z.; Nakajima, A.; Watanabe, T.; Hashimoto, K. Effects of Surface Structure on the Hydrophobicity and Sliding Behavior of Water Droplets. *Langmuir* **2002**, 18, 5818-5822.
30. Kamusewitz, H.; Possart, W.; Paul, D. The relation between Young's equilibrium contact angle and the hysteresis on rough paraffin wax surfaces. *Colloids and Surfaces A: Physicochemical and Engineering Aspects* **1999**, 156, 271-279.
31. Tuteja, A.; Choi, W.; Mabry, J. M.; McKinley, G. H.; Cohen, R. E. Robust omniphobic surfaces. *Proc. Natl. Acad. Sci. U. S. A.* **2008**, 105, 18200-18205.
32. Pan, S.; Kota, A. K.; Mabry, J. M.; Tuteja, A. Superomniphobic Surfaces for Effective Chemical Shielding. *J. Am. Chem. Soc.* **2013**, 135, 578-581.
33. Young, T. An Essay on the Cohesion of Fluids. *Philos. Trans. R. Soc. London* **1805**, 95, 65-87.
34. Poetes, R.; Holtzmann, K.; Franze, K.; Steiner, U. Metastable Underwater Superhydrophobicity. *Physical Review Letters* **2010**, 105, 166104.
35. Koch, K.; Bhushan, B.; Jung, Y. C.; Barthlott, W. Fabrication of artificial Lotus leaves and significance of hierarchical structure for superhydrophobicity and low adhesion. *Soft Matter* **2009**, 5, 1386-1393.
36. Gao, L.; McCarthy, T. J. The "Lotus Effect" Explained: Two Reasons Why Two Length Scales of Topography Are Important. *Langmuir* **2006**, 22, 2966-2967.
37. Herminghaus, S. Roughness-induced non-wetting. *Europhys. Lett.* **2000**, 52, 165-170.
38. Srinivasan, S.; Chhatre, S. S.; Mabry, J. M.; Cohen, R. E.; McKinley, G. H. Solution spraying of poly(methyl methacrylate) blends to fabricate microtextured, superoleophobic surfaces. *Polymer* **2011**, 52, 3209-3218.
39. Verho, T.; Korhonen, J. T.; Sainiemi, L.; Jokinen, V.; Bower, C.; Franze, K.; Franssila, S.; Andrew, P.; Ikkala, O.; Ras, R. H. A. Reversible switching between superhydrophobic states on a hierarchically structured surface. *Proceedings of the National Academy of Sciences* **2012**, 109, 10210-10213.

40. Marmur, A. Wetting on Hydrophobic Rough Surfaces: To Be Heterogeneous or Not To Be? *Langmuir* **2003**, 19, 8343-8348.
41. He, B.; Patankar, N. A.; Lee, J. Multiple Equilibrium Droplet Shapes and Design Criterion for Rough Hydrophobic Surfaces. *Langmuir* **2003**, 19, 4999-5003.
42. Choi, W.; Tuteja, A.; Chhatre, S.; Mabry, J. M.; Cohen, R. E.; McKinley, G. H. Fabrics with Tunable Oleophobicity. *Adv. Mater.* **2009**, 21, 2190-2195.
43. Bormashenko, E.; Pogreb, R.; Whyman, G.; Erlich, M. Cassie−Wenzel Wetting Transition in Vibrating Drops Deposited on Rough Surfaces: Is the Dynamic Cassie−Wenzel Wetting Transition a 2D or 1D Affair? *Langmuir* **2007**, 23, 6501-6503.
44. Chhatre, S. S.; Choi, W.; Tuteja, A.; Park, K.-C.; Mabry, J. M.; McKinley, G. H.; Cohen, R. E. Scale Dependence of Omniphobic Mesh Surfaces. *Langmuir* **2010**, 26, 4027-4035.
45. Cheng, Y.-T.; Rodak, D. E. Is the lotus leaf superhydrophobic? *Appl. Phys. Lett.* **2005**, 86, 144101.
46. Marmur, A. From Hygrophilic to Superhygrophobic: Theoretical Conditions for Making High-Contact-Angle Surfaces from Low-Contact-Angle Materials. *Langmuir* **2008**, 24, 7573-7579.
47. Yang, H.; Zhang, X.; Cai, Z.-Q.; Pi, P.; Zheng, D.; Wen, X.; Cheng, J.; Yang, Z.-R. Functional silica film on stainless steel mesh with tunable wettability. *Surf. Coat. Technol.* **2011**, 205, 5387-5393.
48. Chappuis, J.; Georges, J.-M. Contribution to Study of Wetting - Analysis of a Measuring Method. *J. Chim. Phys. Phys.-Chim. Biol.* **1974**, 71, 567-575.
49. Lewandowski, F. Y.; Dupuis, D. Dynamic measurements of surface tension of solutions of polyisobutylene in mixtures of polybutene oil and Decalin. *J. Non-Newton. Fluid Mech.* **1994**, 52, 233-248.
50. Park, J.; Lyons, C. S.; Strobel, M.; Ulsh, M.; Kinsinger, M. I.; Prokosch, M. J. Characterization of non-uniform wettability on flame-treated polypropylene-film surfaces. *Journal of Adhesion Science and Technology* **2003**, 17, 643-653.
51. Berg, J. C., *An introduction to interfaces & colloids : the bridge to nanoscience*. World Scientific: Hackensack, NJ, 2010.
52. Bonn, D.; Eggers, J.; Indekeu, J.; Meunier, J.; Rolley, E. Wetting and spreading. *Rev. Mod. Phys.* **2009**, 81, 739-805.
53. Mabry, J. M.; Vij, A.; Iacono, S. T.; Viers, B. D. Fluorinated Polyhedral Oligomeric Silsesquioxanes (F-POSS). *Angew. Chem. Int. Ed.* **2008**, 47, 4137-4140.